Defect and Dopant Properties of the $SrCeO_3$-Based Proton Conductor

Glenn C. Mather*,† and M. Saiful Islam‡

Instituto de Cerámica y Vidrio, CSIC, Cantoblanco, 28049 Madrid, Spain, and Chemistry Division, SBMS, University of Surrey, Guildford, GU2 7XH, U.K.

Received November 19, 2004. Revised Manuscript Received January 27, 2005

Atomic-scale studies using advanced simulation techniques have investigated the energetics of defects, oxygen migration, and dopant incorporation in the proton-conducting $SrCeO_3$ system. The interatomic potential model first reproduces the observed distorted perovskite structure of $SrCeO_3$. Substitution with trivalent dopants (M) on the A site in $SrCe(Yb)O_{3-\delta}$ (via $V_o^{\bullet\bullet}$ consumption) is compared with substitution on the B site (via $V_o^{\bullet\bullet}$ creation); the results support the premise that the absence of ionic conductivity at low doping levels is associated with dopant partitioning over both A and B sites. Dopant-vacancy association is predicted to occur in $SrCe_{0.9}M_{0.1}O_{2.95}$ for a wide range of M cations. Formation of ($M'_{Ce}-OH_o^{\bullet}$) clusters is also calculated to be favorable in accordance with reported proton-trapping effects. The lowest $M'_{Ce}-OH_o^{\bullet}$ binding energies and the largest M−H distances are found for the most common dopants for proton conductivity in the $SrCeO_3$ system, namely, Y and Yb. The pathway for oxygen migration is proposed as a curved trajectory with an asymmetric energy distribution. The lowest energy redox process is calculated to be oxidation with the formation of holes in accordance with the observation of p-type conductivity at increasing oxygen partial pressures (pO_2).

1. Introduction

Studies of high-temperature proton conductors (HTPC) have intensified in the last 10 years as the extensive and important contribution that these materials could make to fuel cell and other electrochemical applications is more widely recognized.[1−6] For example, the processes which form the basis of the hydrogen economy (production, separation, and oxidation of hydrogen) may be carried out employing a proton-conducting ceramic oxide.

Conversion of hydrogen using a solid oxide fuel cell (SOFC) with a proton-conducting electrolyte (protonic ceramic fuel cell, PCFC) occurs at an intermediate temperature (400−800 °C) without expensive electrocatalysts or necessity to recirculate the fuel.[7] Additional advantages, generally associated with oxide-ion-based SOFCs, include modularity of structure and cogeneration of heat and electricity. The use of HTPC materials as hydrogen and humidity sensors,[8−11] chemical reactors for ammonia generation,[12] partial oxidation[13] and reforming[14] of methane, and electrochemical promotion of oxidation[15] has also been investigated. However, bringing these technologies to the marketplace is likely to require improvement in the electrical and materials' properties.

The most well-known HTPC materials are the perovskite oxides (ABO_3) with large basic A cations (e.g., Ba, Sr) and tetravalent B cations (e.g., Zr, Ce) first discovered to conduct protons by Iwahara and co-workers.[16−18] The perovskites incorporate protons when doped with a lower valence cation on the B site ("acceptor doped") with hydroxyl groups from the water filling the oxygen vacancies, $V_o^{\bullet\bullet}$ (in Kröger-Vink notation):

$$H_2O + O_o^{\times} + V_o^{\bullet\bullet} \rightarrow 2OH_o^{\bullet} \quad (1)$$

At high temperature, desorption of water takes place, often accompanied by migration of oxygen vacancies in the crystal lattice. In oxidizing atmospheres, the oxygen vacancies may, instead, be compensated by formation of holes:[19,20]

* To whom correspondence should be addressed.
† CSIC.
‡ University of Surrey.

(1) Iwahara, H. *Solid State Ionics* **1988**, *28−30*, 573.
(2) Iwahara, H.; Asakura, Y.; Katahira K.; Tanaka, M. *Solid State Ionics* **2004**, *168*, 299.
(3) Iwahara, H. *Solid State Ionics* **1995**, *77*, 289.
(4) Norby, T. *Solid State Ionics* **1999**, *125*, 1.
(5) Bonanos, N. *Solid State Ionics* **1992**, *53−56*, 967.
(6) Kreuer, K. D. *Annu. Rev. Mater. Res.* **2003**, *33*, 333.
(7) Coors, W. G. *J. Power Sources* **2003**, *118*, 150.
(8) Matsumoto, H.; Suzuki, T.; Iwahara, H. *Solid State Ionics* **1999**, *116*, 99.
(9) Iwahara, H.; Uchida, H.; Ogaki, K.; Nagato, H. *J. Electrochem. Soc.* **1991**, *138*, 295.
(10) De Schutter, F.; Vangrunderbeek, J.; Luyten, J.; Kosacki, I.; Van Landschoot, R.; Schram, J.; Schoonman, J. *Solid State Ionics* **1992**, *57*, 77.
(11) Hassen, M. A.; Clarke, A. G.; Swetnam, M. A.; Kumar, R. V.; Fray, D. J. *Sens. Actuators* **2000**, *B69*, 138.
(12) Marnellos, G.; Stoukides, M. *Science* **1998**, *282*, 98.
(13) Asano, K.; Hibino, T.; Iwahara, H. *J. Electrochem. Soc.* **1995**, *142*, 3241.
(14) Hibino, T.; Hamakawa, S.; Suzuki, T.; Iwahara, H. *J. Appl. Electrochem.* **1994**, *24*, 126.
(15) Thursfield, A.; Brosda, S.; Pliangos, C.; Schöber, T.; Vayenas, C. G. *Electrochim. Acta* **2003**, *48*, 3779.
(16) Iwahara, H.; Esaka, T.; Uchida, H.; Maeda, N. *Solid State Ionics* **1981**, *3−4*, 359.
(17) Iwahara, H.; Uchida, H.; Kondo, K.; Ogaki, K. *J. Electrochem. Soc.* **1988**, *135*, 529.
(18) Yajima, T.; Kazeoka, H.; Yogo, T.; Iwahara, H. *Solid State Ionics* **1991**, *47*, 271.

10.1021/cm047976l CCC: $30.25
Published on Web 03/09/2005

$$^1/_2O_2 + V_o^{\bullet\bullet} \rightarrow O_o^{\times} + 2h^{\bullet} \quad (2)$$

Reduction may also take place at low oxygen partial pressures:[20,21]

$$O_o^{\times} = V_o^{\bullet\bullet} + ^1/_2O_2 + 2e' \quad (3)$$

Hence, the conductivity and defect properties are highly dependent on atmosphere and temperature. Implementation of HTPC materials in devices therefore requires careful mapping of the conditions and the defect chemistry required for pure protonic conductivity (for sensor applications), mixed proton and n-type conductivity (for H_2-separation membranes), and mixed proton and oxide-ion conductivity (for steam diffusion).

Perovskites based on $SrCeO_3$, doped with Yb or Y, offer more moderate levels of proton conductivity in comparison to the Ba-containing analogues but with much lower oxide-ion conductivity, particularly at high temperature. This is a principal reason for the employment of the $SrCeO_3$ system in HTPC-based sensor and membrane applications, developed principally by Iwahara.[10,11,22−26] Accordingly, $SrCeO_3$-based phases have also attracted considerable attention in numerous fundamental studies of protons in solids.[27−32]

$SrCeO_3$ crystallizes with the $GdFeO_3$-type perovskite structure,[33,34] which is distorted from the cubic prototype as a result of the mismatch in size between a small A cation and large B cation. The distortion in $SrCeO_3$ is one of the most pronounced observed, with a tolerance factor (t = 0.886) at the lower limit for perovskites.[35] The migration pathways for the oxide ion are more anisotropic in the distorted cell, which may account for the lower oxide-ion transport numbers of $SrCeO_3$-based phases in comparison to the $BaCeO_3$-based system.[34]

A greater fundamental understanding of the defect chemistry at the microscopic level, which underpins the highly attractive properties of the $SrCeO_3$ system, is of considerable importance. Atomistic simulation techniques are well-suited to studying defect properties on the atomic- and nanoscale,[36−39] as demonstrated in previous successful studies of the ceramic proton conductors $AZrO_3$ (A = Ca, Sr)[38,40] and $BaCeO_3$.[39,41] In this paper we address a number of important topics concerning the $SrCeO_3$-based proton conductor using, for the first time, a comprehensive sequence of atomistic simulations. Emphasis here is placed on investigating the energetic and mechanistic features of intrinsic defects, dopant site selectivity, defect association, proton incorporation, and oxide-ion migration.

Table 1. Interatomic Potentials for $SrCeO_3$

(i) Buckingham Potentials (Cutoff, 15 Å) and Lattice Energies of Component Oxides

interaction	A (eV)	ρ (Å)	C (eV Å^6)	U_L (eV)	ref
$Sr^{2+}\cdots O^{2-}$	1400.0	0.34535	0.00	−33.42	43
$Ce^{4+}\cdots O^{2-}$	1986.833	0.35107	20.40	−105.66	41, 44
$O^{2-}\cdots O^{2-}$	22764.3	0.1490	43.84		41

(ii) Shell Model[a]

species	Y (e)	k (eV Å^{-2})	ref
Sr^{2+}	1.33	21.53	43
Ce^{4+}	7.70	291.0	41, 44
O^{2-}	−2.389	42.0	41

[a] Y and k refer to the shell charge and harmonic force constant, respectively.

2. Simulation Methodology and Structural Models

2.1. Methods. Only a short review of the technique will be given here (embodied within the GULP code[42]) since comprehensive reviews have been given elsewhere.[36]

The basis of the lattice simulation is the specification of the potential energy of the system in terms of atomic coordinates. Both perfect and defect lattices are described by the Born model, in which the potential energy is partitioned into long-range Coulombic terms and short-range pair potentials of the Buckingham form

$$V_{ij} = A_{ij} \exp(-r/\rho_{ij}) - C_{ij}/r^6 \quad (4)$$

where the parameters A_{ij}, ρ_{ij}, and C_{ij} are assigned to ion−ion interactions. The potential parameters used in this study, listed in Table 1, were mostly taken from previous simulation studies[41,43,44] with minor refinement of the ρ parameter for the Sr−O interaction using the experimental crystal structure. The polarizability of the ions which arises from charged defects in the lattice must also be incorporated into the potential model. The shell model developed by Dick and Overhauser[45] treats the polarization of each ion in

(19) Bonanos, N.; Ellis, B.; Mahmood, M. N. *Solid State Ionics* **1988**, *28−30*, 579.
(20) Kosacki, I.; Tuller, H. L. *Solid State Ionics* **1995**, *80*, 223.
(21) Song, S. J.; Wachsman, E. D.; Dorris, S. E.; Balachandran, U. *J. Electrochem. Soc.* **2003**, *150*, A1484.
(22) Iwahara, H.; Esaka, T.; Uchida, H.; Yamauchi, T.; Ogaki, K. *Solid State Ionics* **1986**, *18−19*, 1003.
(23) Hamakawa, S.; Li, L.; Li, A.; Iglesia E. *Solid State Ionics* **2002**, *48*, 71.
(24) Matsumoto, H.; Okubo, M.; Hamajima, S.; Katahira, K.; Iwahara, H. *Solid State Ionics* **2002**, *152−153*, 715.
(25) Iwahara, H.; Uchida, H.; Tanaka, S. *Solid State Ionics* **1983**, *9*, 1021.
(26) Mather, G. C.; Figueiredo, F. M.; Fagg, D. P.; Norby, T.; Jurado, J. R.; Frade, J. R. *Solid State Ionics* **2003**, *158*, 333.
(27) Karmonik, C.; Udovic, T. J.; Paul, R. L.; Rush, J. J.; Lind, K.; Hempelmann, R. *Solid State Ionics* **1998**, *109*, 207.
(28) Matzke, Th.; Stimming, U.; Karmonik, Ch.; Soetratmo, M.; Hempelmann, R.; Güthoff, F. *Solid State Ionics* **1996**, *86−88*, 621.
(29) Hempelmann, R.; Karmonik, Ch.; Matzke, Th.; Cappadonia, M.; Stimming, U.; Springer, T.; Adams, M. A. *Solid State Ionics* **1995**, *77*, 152.
(30) Krug, F.; Schöber, T.; Paul, R.; Springer, T. *Solid State Ionics* **1995**, *77*, 185.
(31) Maekawa, H.; Kashii, N.; Kawamura, J.-I.; Hinatsu, Y.; Yamamura, T. *Solid State Ionics* **1999**, *122*, 231.
(32) Taherparvar, H.; Kilner, J. A.; Baker, R. T.; Sahibzada, M. *Solid State Ionics* **2003**, *162−163*, 297.
(33) Ranløv, J.; Lebech, B.; Nielsen, K. *J. Mater. Chem.* **1995**, *5*, 743.
(34) Knight, K. S.; Bonanos, N. *Mater. Res. Bull.* **1995**, *30*, 347.
(35) Yokokawa, H.; Kawada, T.; Dokiya, M. *J. Am. Ceram. Soc.* **1989**, *72*, 152.
(36) Catlow, C. R. A. In *Solid State Chemistry: Techniques*; Cheetham, A. K., Day, P., Eds.; Clarendon Press: Oxford, 1987.
(37) Islam, M. S. *Solid State Ionics* **2002**, *154−155*, 75.
(38) Islam, M. S.; Slater, P. R.; Tolchard, J. R.; Dinges, T. *Dalton Trans.* **2004**, 3061.
(39) Wu, J.; Davies, R. A.; Islam, M. S.; Haile, S. M. *Chem. Mater*. **2005**, *17*, 846.
(40) Davies, R. A.; Islam, M. S.; Gale, J. D. *Solid State Ionics* **1999**, *126*, 323.
(41) Glöckner, R.; Islam, M. S.; Norby, T. *Solid State Ionics* **1999**, *122*, 145.
(42) Gale, J. D. *J. Chem. Soc., Faraday Trans.* **1997**, *97*, 33.
(43) Lewis, G. V.; Catlow, C. R. A. *J. Phys. C, Solid State Phys.* **1985**, *18*, 1149.
(44) Balducci, G.; Islam, M. S.; Kaspar, J.; Fornasiero, P.; Graziani, M. *Chem. Mater.* **2000**, *12*, 677.
(45) Dick, B. G.; Overhauser, A. W. *Phys. Rev.* **1958**, *112*, 90.

Table 2. Parameters for the O−H Interaction

Morse potential (intramolecular)	D (eV)	β (Å^{-1})	r_o (Å)
O···H	7.0525	2.1986	0.9485
Buckingham potential (intermolecular)	A (eV)	ρ (Å)	C (eV Å^6)
O···H	311.97	0.2500	0

terms of a core (representing the nucleus and core electrons) connected to a shell (representing the valence electrons) via a harmonic spring. The shell model has been shown to simulate effectively both dielectric and elastic properties of polar solids by including the vital coupling between the short-range repulsive forces and electronic polarization.

Lattice relaxation around a charged defect (e.g., oxygen vacancy or cation dopant) causes considerable perturbation of the surrounding lattice. The calculation of the energy associated with the defect is performed by the two-region Mott-Littleton approach,[46] in which the lattice is partitioned into inner and outer spherical regions centered on the defect. Ions in the inner region are relaxed explicitly (in this study, more than 530 atoms). The remainder of the crystal (>3000 ions), where the defect forces are relatively weaker, are treated by more approximate quasi-continuum methods. Local relaxation is effectively modeled, therefore, rather than considering the crystal as a rigid lattice through which ion species diffuse.

The O−H interaction was modeled using an attractive Morse potential (with Coulomb subtraction)

$$V(r) = D\{1 - \exp[-\beta(r - r_o)]\}^2 \quad (5)$$

using parameters (Table 2) developed from ab initio quantum mechanical cluster calculations,[47] with a point charge representation of the surrounding lattice. The dipole moment of the O−H group was simulated by placing charges of −1.4263 and +0.4263 on the O and H species, respectively (overall charge −1) in accordance with this study.[47] Additional Buckingham parameters were employed to simulate the interaction of the lattice oxygens with the hydroxyl unit.[48] This approach has been employed successfully in previous studies of protons in $AZrO_3$ and $BaCeO_3$ perovskites.[40,41]

2.2. Structural Modeling of $SrCeO_3$ and $SrCe_{0.9}Yb_{0.1}O_{2.95}$. The unit-cell parameters and ion positions of the distorted orthorhombic structure of $SrCeO_3$ were first optimized (energy minimized) under constant pressure conditions, allowing both unit-cell parameters and atomic positions to relax. On relaxation, the potentials successfully reproduced the observed structure as indicated by the slight changes from experimental X-ray values[49] in the unit-cell parameters (<1%) and the bond lengths (Table 3). Additional experimental data on dielectric and elastic properties are currently unavailable, but would be useful for further validation and refinement of the potential models.

To observe significant levels of proton conductivity in perovskite oxides, partial substitution of the B cation with a lower valence dopant is required for the formation of oxygen vacancies and their hydration to incorporate mobile protons (eq 1). In this study, we also investigated the Yb-doped system, $SrCe_{0.9}Yb_{0.1}O_{2.95}$, since this is a commonly used dopant and a suitable representative doping level within our supercell approach. The supercell (1 × 1 × 5) of the $SrCeO_3$ unit cell was constructed in space group $P1$; the lattice energy of the supercell was −139.82 eV/formula unit, equivalent to that of the (single) unit-cell simulation of $SrCeO_3$ (Table 1).

Table 3. Calculated and Experimental Properties of $SrCeO_3$

Property		
lattice energy (eV per formula unit)		−139.82
Unit-Cell Parameters (Å)		
	experimental[49]	calculated	difference (%)
a	6.1312	6.0744	0.92
b	8.6504	8.5421	1.25
c	5.9944	5.9834	0.18
Bond Lengths (Å)			
bond	experimental[49]	calculated	difference (%)
Ce−O1 ×2	2.26	2.21	2.21
Ce−O2 ×2	2.22	2.20	0.90
Ce−O2 ×2	2.25	2.21	1.78
Sr−O1 ×1	2.46	2.50	−1.62
Sr−O1 ×1	2.61	2.73	−4.60
Sr−O2 ×2	2.51	2.51	0.00
Sr−O2 ×2	2.86	2.96	−3.50
Sr−O2 ×2	3.06	3.04	0.65

Table 4. Lattice Energy of Various Defect Configurations for the $SrCe_{0.9}Yb_{0.1}O_{2.95}$ Supercell Structures

configuration[a]	per supercell unit (eV)	per formula unit (eV)
(i) $Yb_{Ce}'V_{O2}^{\bullet\bullet}Yb_{Ce}'$ trimer	−680.20	−136.04
(ii) $Yb_{Ce}'V_{O2}^{\bullet\bullet}$pair + next-nearest Yb	−679.85	−135.97
(iii) $Yb_{Ce}'V_{O2}^{\bullet\bullet}$pair + isolated Yb	−679.70	−135.94
(iv) Yb_{Ce}', $V_O^{\bullet\bullet}$, Yb_{Ce}' at isolated positions	−679.40	−135.88

[a] Figure 1.

The stoichiometry of the supercell was then set to $Sr_{20}Ce_{18}Yb_2O_{59}$ ($SrCe_{0.9}Yb_{0.1}O_{2.95}$), by placing the two Yb atoms and one O vacancy in the three configurations shown schematically in Figure 1. These correspond to (i) nearest-neighbor positions to form a ($Yb_{Ce}'V_o^{\bullet\bullet}Yb_{Ce}'$) trimer, (ii) a ($Yb_{Ce}'V_o^{\bullet\bullet}$) nearest-neighbor pair with a next-nearest Yb, and (iii) a ($Yb_{Ce}'V_o^{\bullet\bullet}$) nearest-neighbor pair with Yb at the furthest possible distance from the pair cluster; finally, a fourth configuration (iv) was also considered consisting of all three defects as far apart as possible. The lattice energy per formula unit for each of these configurations is listed in Table 4.

The lowest energy configuration is associated with the next-nearest neighbor defects ($Yb_{Ce}'V_o^{\bullet\bullet}Yb_{Ce}'$) trimer, centered on O1 or O2 sites, and the highest energy for the configuration with isolated defects. We recognize that the energy differences are small but note that alternative orientations for the same configurations gave similar results. The supercell simulation thus predicts that dopant clusters may form in $SrCe_{0.9}Yb_{0.1}O_{2.95}$, a point we return to below. Our defect calculations on the $SrCe_{0.9}Yb_{0.1}O_{2.95}$ system will therefore focus on this favored supercell configuration with calculated unit-cell parameters: a = 6.0733, b = 8.5055, c = 29.9031 Å.

3. Results and Discussion

3.1. Intrinsic Atomic Defects. The energies of isolated intrinsic defects (vacancies and interstitials) in $SrCeO_3$ and $SrCe_{0.9}Yb_{0.1}O_{2.95}$ were first evaluated (Table 5a). Frenkel- and Schottky-type defect energies were calculated from the isolated defect energies (Table 5b). The lattice energies used in the calculation of Schottky-type defects were obtained from atomic simulations of SrO,[43] CeO_2,[44] and the $SrCeO_3$-based phases (Tables 3 and 4).

Inspection of Table 5a reveals that oxygen vacancies have similar energies for both O1 and O2 sites in $SrCeO_3$.

(46) Mott, N. F.; Littleton, M. J. *Trans. Faraday Soc.* **1938**, *34*, 485.
(47) Saul, P.; Catlow, C. R. A. *Philos. Mag. B* **1985**, *51*, 107.
(48) Schröder, K. P.; Sauer, J.; Leslie, M.; Catlow, C. R. A.; Thomas, J. M. *Chem. Phys. Lett.* **1992**, *188*, 320.
(49) Mather, G. C.; Jurado, J. R. *Bol. Soc. Esp. Cerám. Vidrio* **2003**, *42*, 311.

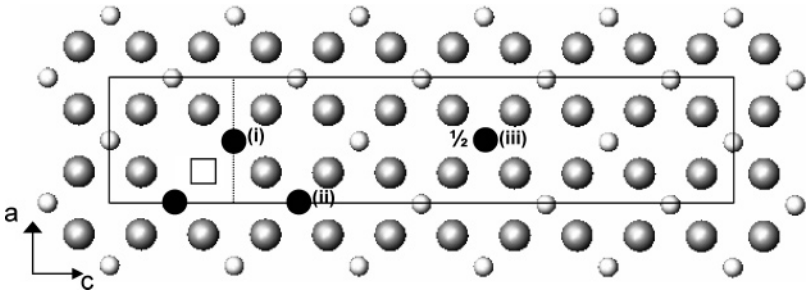

Figure 1. Supercell and defect configurations of Yb-doped $SrCeO_3$. Projection of a $1 \times 1 \times 5$ supercell of $SrCeO_3$ projected onto the *ac* plane (orthorhombic distortion not represented; Ce as small white spheres and O as gray spheres). Placement of two Yb dopant cations (black spheres) and an oxygen vacancy (square) as (i) ($Yb_{Ce}'V_o^{\bullet}Yb_{Ce}'$) nearest-neighbor positions (trimer), (ii) ($Yb_{Ce}'V_o^{\bullet}$) pair with next-nearest Yb, and (iii) ($Yb_{Ce}'V_o^{\bullet}$) pair and isolated Yb at $y = {}^1/_2$.

Table 5. Calculated Defect Energies in $SrCeO_3$ and $SrCe_{0.9}Yb_{0.1}O_{2.95}$

(a) Isolated Point Defects (in eV)

		$SrCe_{0.9}Yb_{0.1}O_{2.95}$	
defect	$SrCeO_3$	adjacent to trimer	isolated from trimer
Sr vacancy	21.23	20.89	21.21
Ce vacancy	81.58	81.11	81.36
O(1) vacancy	19.99	19.35	20.02
O(2) vacancy	19.98	18.57	20.03
Sr interstitial	−10.52		−10.47
Ce interstitial	−57.95		−62.01
O interstitial	−11.02		−11.05

(b) Frenkel- and Schottky-Type Disorder (eV/defect)

type	defect equilibrium	$SrCeO_3$	$SrCe_{0.9}Yb_{0.1}O_{2.95}$
Sr Frenkel	$Sr_{Sr}^{\times} = V_{Sr}'' + Sr_i^{\bullet\bullet}$	5.36	5.21
Ce Frenkel	$Ce_{Ce}^{\times} = V_{Ce}^{4\prime} + Ce_i^{4\bullet}$	11.81	9.55
O Frenkel	$O_o^{\times} = V_o^{\bullet\bullet} + O_i''$	4.48	3.76
Schottky	$Sr_{Sr}^{\times} + Ce_{Ce}^{\times} + 3O_o^{\times} = V_{Sr}'' + V_{Ce}^{4\prime} + 3V_o^{\bullet\bullet} + SrCeO_3$	4.57	3.58
Sr−O vacancy pair	$Sr_{Sr}^{\times} + O_o^{\times} = V_{Sr}'' + V_o^{\bullet\bullet} + SrO$	3.90	3.02
Ce−O vacancy trimer	$Ce_{Ce}^{\times} + 2O_o^{\times} = V_{Ce}^{4\prime} + 2V_o^{\bullet\bullet} + CeO_2$	5.45	4.31

However, oxygen vacancies in the Yb-containing systems placed adjacent to the ($Yb_{Ce}'V_o^{\bullet\bullet}Yb_{Ce}'$) trimer have lower energy than those isolated from the trimer, with the lowest value obtained for the O2 site. In a neutron diffraction study of $SrCe_{0.95}Yb_{0.05}O_{2.975}$, the oxygen site occupancies could not be refined but a better fit was obtained with the vacancy on the O2 site in comparison to a random vacancy distribution.[34] In contrast, neutron structure refinement of an Y-doped system, $SrCe_{0.85}Y_{0.15}O_{2.925}$, suggested location of the vacancy on the O1 site.[33]

Frenkel defects are associated with considerable amounts of energy, as is expected in the close-packed perovskite structure. The most favorable intrinsic defect in $SrCeO_3$ and Yb-doped $SrCeO_3$ is the SrO vacancy pair, with a lower energy in the doped system. However, the magnitude of the energies suggests a relatively low concentration of such defects. This disorder is less favorable than that in the related $BaCeO_3$ system,[41] which is compatible with the greater volatility of BaO at high temperature with respect to SrO.

3.2. Dopant-Ion Substitution. The substitution of a range of trivalent cations was investigated on both Sr and Ce sites for the $SrCeO_3$ and $SrCe_{0.9}Yb_{0.1}O_{2.95}$ lattices in order to gain some insight into the relative energetics of dopant incorporation. Substitution of the trivalent cation on the Ce site was analyzed according to the standard "acceptor-doping" defect reaction, with the creation of oxygen vacancies as charge-compensating defects:

$$ {}^1/_2M_2O_3 + Ce_{Ce}^{\times} + {}^1/_2O_o^{\times} = M_{Ce}' + CeO_2 + {}^1/_2V_o^{\bullet\bullet} \quad (6) $$

For substitution on the Sr site, two possible compensation mechanisms were investigated, corresponding to the creation of cation vacancies

$$ {}^1/_2M_2O_3 + {}^3/_2Sr_{sr}^{\times} = M_{Sr}^{\bullet} + {}^1/_2V_{Sr}'' + {}^3/_2SrO \quad (7) $$

and the consumption or "filling" of oxygen vacancies in the $SrCe_{0.9}Yb_{0.1}O_{2.95}$ system:

$$ {}^1/_2M_2O_3 + Sr_{sr}^{\times} + {}^1/_2V_o^{\bullet\bullet} = M_{Sr}^{\bullet} + SrO + {}^1/_2O_o^{\times} \quad (8) $$

The energies of "solution" of the above reactions were evaluated by combining the corresponding defect and lattice energy terms.[43,44,50] This provides a systematic analysis of the relative energies of different dopant species at the same site and, in the case of substitution at the A-site, of the preferred compensation mechanism. Calculation of the solution energies for $SrCe_{0.9}Yb_{0.1}O_{2.95}$ was based on the lowest-energy trimer configuration; point-defect energies of M_{Ce}' and $M_{Sr}^{\bullet}$ were then taken for a position isolated from the trimer. The interatomic potentials for the dopant cations were taken as those corresponding to the binary metal oxides[43,50] as used in previous successful studies of dopants in perovskite oxides.[37−41] The resulting solution energies for substitution on the A and B sites as a function of ionic radius[51] in both $SrCeO_3$ and $SrCe_{0.9}Yb_{0.1}O_{2.95}$ are shown in Figure 2. Several interesting observations may be made from the results (we emphasize trends rather than absolute values due to the large magnitude of the employed lattice energies).

Examination of Figure 2 reveals a degree of correlation with ion size in which the lowest calculated solution energy infers a preferential substitution. For undoped $SrCeO_3$, energies of solution of the dopants on the Ce site are lower than the energies on the Sr site. The dopants most commonly used for acceptor doping in the $SrCeO_3$-based series, namely, Yb and Y, are those with the lowest Ce-site solution energy. Occupation of the Ce site with La has a much higher energy.

(50) Freeman, G. M.; Catlow, C. R. A. *J. Solid State Chem.* **1990**, *85*, 65.
(51) Shannon, R. D. *Acta Crystallogr.* **1976**, *A32*, 751.

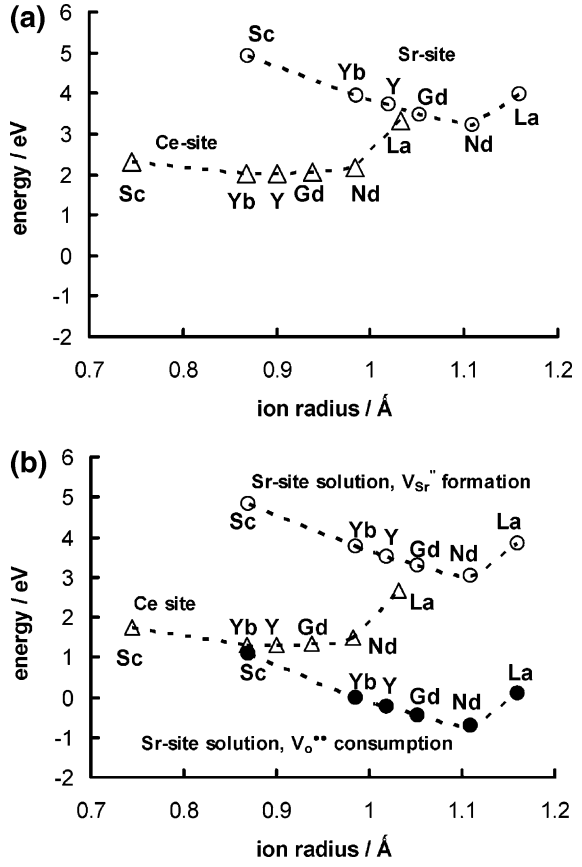

Figure 2. Calculated solution energies for trivalent dopants (M^{3+}) as a function of dopant ionic radius using 8-fold and 6-fold coordination environments for Sr and Ce sites, respectively (dashed lines are guides for the eye). (a) $SrCeO_3$: substitution on the Sr site via eq 7; substitution on the Ce site via eq 6. (b) $SrCe_{0.9}Yb_{0.1}O_{2.95}$: substitution on the Sr site via eqs 7 and 8; substitution on the Ce site via eq 6.

We may note that similar calculations for Ce^{3+} (employing the lattice energy for Ce_2O_3[44]) indicate that this cation also shows a low solution energy at the Sr site.

However, in the Yb-doped system, $SrCe_{0.9}Yb_{0.1}O_{2.95}$, in which oxygen vacancies are already present, the solution energies for substitution on the Sr site (compensated by the consumption of oxygen vacancies via reaction 8) are lower than the energies of solution on the Ce site. That is to say, the M^{3+} dopants (particularly Nd and Gd) are predicted to show a preference for the Sr site at the dilute limit. "Amphoteric" behavior with partitioning of the dopant over both Sr and Ce sites is, therefore, predicted.

We note that substitution is expected to take place predominantly on the Ce site at moderately high doping levels according to the starting ratio of component oxides (and experimental observation, e.g., for $M \geq 5$ at. %). Oxygen vacancies are not created when the M cation is distributed equally between the Sr and Ce sites (eqs 6 and 8), which, in turn, would lead to lower proton uptake. This is consistent with proposals to explain the "threshold effect" in strontium cerate perovskites whereby ionic and p-type conductivity is not observed at low doping levels (ca. 2 at. %) due to possible partitioning of the dopant over both cation sites.[52,53] At higher doping concentrations, a greater proportion of trivalent cation occupies the Ce site, according to the requirements of the nominal stoichiometry, forming oxygen vacancies (eq 6) which may then be compensated by mobile protons. Whereas doping on the Ce site is accommodated by Ce substoichiometry (as in $SrCe_{0.9}Yb_{0.1}O_{3-\delta}$), partial occupation of the M^{3+} dopant on the Sr site implies segregation of an equivalent amount of SrO according to eq 8. The presence of excess SrO (e.g., in grain boundaries) is sometimes assumed to result in degradation of sintered bodies on carbonation and the importance of careful synthesis has been highlighted.[54] We may also note, however, that recent studies suggest the possible accommodation of moderate amounts of excess SrO in the bulk in nominally stoichiometric $SrCeO_3$ (with CeO_2 as a second phase) by a mechanism which is not apparent at the resolution of the X-ray structure.[49,55]

Solid-solution formation has recently been reported in the Sr-deficient $Sr_{1-x}Ce(M)O_{3-\delta}$ (M = Gd, Yb) series,[56] whereas single-phase, Sr-deficient material of nominal composition $Sr_{1-x}CeO_{3-x}$ could not be synthesized.[49] It follows that Sr deficiency in the doped series is likely to be compensated by partitioning of the dopant over both cation sites. Haile et al.[39,57] indicate that Ba deficiency in the $BaCeO_3$ system shifts dopant incorporation onto the Ba site, with significant Nd dopant partitioning over both Ba and Ce sites, leading to reduced proton uptake and lower proton conductivity.

The unit-cell parameters for $Sr_{1-x}Ce(M)O_{3-\delta}$ (M = Gd, Yb) exhibit an anomalous variation with Sr deficiency (x), in common with a number of other cerate perovskite solid solutions.[56] The origin of this apparently widespread phenomenon is unknown at present but is proposed to result from alleviation of lattice strain or variations in the oxygen-vacancy (and proton) content and/or related defect association. Dopant partitioning over both Sr and Ce sites decreases the vacancy content with increasing Sr deficiency (eq 8) but the presence of M dopant on the Sr site may equally influence the lattice distortion.

3.3. Oxide-Ion Migration. The oxygen vacancies required for incorporation of protons may also migrate, particularly at high temperature (>600 °C) when the exothermic absorption of water is no longer favored (eq 1). Whereas oxygen transport may be disadvantageous for certain applications, steam permeation (involving simultaneous diffusion of protons and oxygen vacancies) has been shown to inhibit coking of the anode in a PCFC operating on methane.[7] In this context, atomistic simulation of oxygen migration may greatly assist in our understanding of the mechanistic features of oxygen transport in these systems.

The energy profile of a migrating oxide ion was first calculated by placing the ion at intermediate sites between adjacent oxygen vacancies along edges of a CeO_6 octahedron. The corresponding energies for direct linear migration

(52) Phillips, R. J.; Bonanos, N.; Poulsen, F. W.; Ahlgren, E. O. *Solid State Ionics* **1999**, *125*, 389.
(53) Sammes, N.; Phillips, R.; Smirnova, A. *J. Power Sources* **2004**, *134*, 153.
(54) de Vries, K. J. *Solid State Ionics* **1997**, *100*, 193.
(55) Chavan, S. V.; Tyagi, A.-K. *Thermochim. Acta* **2002** *390*, 79.
(56) Kruth, A.; Mather, G. C.; Jurado, J. R.; Irvine, J. T. S. *Solid State Ionics* **2005**, *176*, 703.
(57) Wu, J.; Li, L, P.; Espinosa, L.; Haile, S. M. *J. Mater. Res.* **2004**, *19*, 2366.

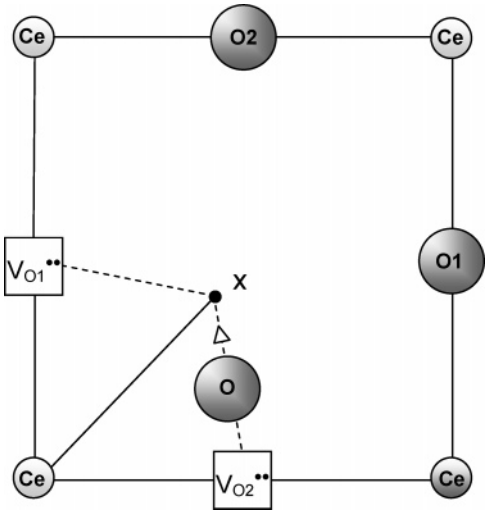

Figure 3. Schematic representation of the calculated pathway (dashed lines) of oxide-ion migration passing through a minimum in energy (×) relative to the Ce atom.

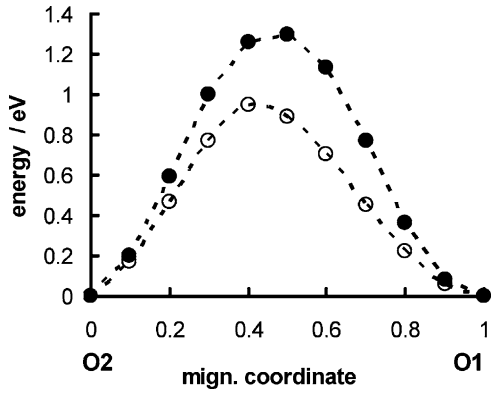

Figure 4. Energy profile of oxygen vacancy migration between O1 and O2 sites along cell edge (closed circles) and curved pathway (open circles).

between two O2 sites and between O2 and O1 sites were calculated as 1.41 and 1.30 eV, respectively. However, previous studies have shown that the lowest energy pathway for oxide-ion migration in several perovskite oxides is not linear, but curved away from the octahedral edge.[37,40,41] We stress that it is often assumed that the migrating ion takes the shortest path between adjacent anion sites (i.e., a direct path along the octahedron edge) and that, to the best of our knowledge, previous experimental investigations have not indicated a nonlinear path.

Hence, to estimate the saddle point of a curved pathway, energies for a migrating oxide ion were calculated on a (solid) line (Figure 3) extending from the midpoint between O1 and O2 vacancies in line with the adjacent Ce atom. The energy of the oxide ion along this line is at a minimum (point × in Figure 3) at approximately 0.3 Å from the midpoint of the octahedral edge. The migration profile between oxygen sites and this energy minimum (shown as a dashed line in Figure 3) is slightly asymmetric with an associated activation energy of 0.95 eV (Figure 4), with the higher energy profile for the linear path also shown for comparison. The asymmetry is likely to result from unequal distances to the neighboring Sr cations in the distorted $SrCeO_3$ structure. It would be interesting to examine this calculated pathway using a similar neutron diffraction analysis employed by

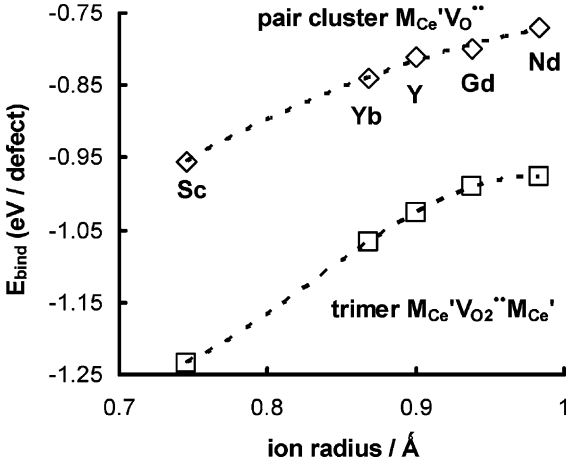

Figure 5. Calculated binding energies (per defect) of dopant-vacancy clusters in $SrCeO_3$ as a function of dopant cation radius.

Yashima et al.,[58] which supported our predicted curved pathway in the $LaGaO_3$-based oxide ion conductor.[37]

Activation energies for oxide-ion transport in $SrCeO_3$-based systems determined experimentally range from 0.67 to 0.77 eV[20,59,60] in the temperature range 600−800 °C. Our calculated value for oxide-ion migration in $SrCeO_3$ (0.95 eV) is higher than that obtained for related atomistic simulation studies of $BaCeO_3$ (0.84 eV for the cubic structure), which is consistent with the observation of higher oxide-ion transport numbers for the Ba-containing phases.

3.4. Dopant-Vacancy Association. The dopant-defect interactions predicted from the supercell calculations of $SrCe_{0.9}Yb_{0.1}O_{2.95}$ may considerably affect the ionic conductivity. Oxide-ion conductivity tends to decrease as the activation energy for vacancy conduction incorporates the binding (association) energy term. This additional term is significant at temperatures below 600 °C for ceria- and zirconia-based oxide-ion conductors, in the range where we may also expect proton conductivity in the HTPC systems. The energies of defect clusters in the $SrCeO_3$ system were calculated for the same range of trivalent dopants in order to assess dopant-vacancy association as a function of dopant ionic radius.

Defect clusters were calculated for (i) simple pair clusters of a neighboring dopant ion and oxygen vacancy ($M_{Ce}'V_o^{\bullet\bullet}$) and (ii) neutral trimer clusters ($M_{Ce}'V_o^{\bullet\bullet}M_{Ce}'$) centered on O1 or O2. Binding energies were then calculated as the difference between the energy of the cluster and the sum of the isolated component defects. Figure 5 shows the calculated binding energies of the possible defect clusters against the ionic radius of the dopant cation. The results suggest that both pair and trimer clusters are favorable defect configurations with the latter associated with stronger binding energies. Pair clusters have equivalent energies for both O1 and O2 vacancies, whereas, for larger ions, trimers based around O2 were found to be slightly more favorable than those centered on O1.

(58) Yashima, M.; Nomura, K.; Kageyama, H.; Miyazaki, Y.; Chitose, N.; Adachi, K. *Chem. Phys. Lett.* **2003**, *380*, 391.
(59) Song, S.-J.; Wachsman, E. D.; Dorris, S. E.; Balachandran, U. *J. Electrochem. Soc.* **2003**, *150*, A790.
(60) Tsuji, T.; Nagano, T. *Solid State Ionics* **2000**, *136−7*, 179.

Table 6. Calculated Parameters for Water Incorporation (E_{H_2O}) and O−H Bond Lengths in $SrCe_{0.9}Yb_{0.1}O_{2.95}$

O−H position	E_{OH} (eV)	E_{H_2O} (eV)	O−H (Å)
O1	14.83	−1.46	0.986
O2	14.77	−0.80	0.986

The above results corroborate the supercell simulation of $SrCe_{0.9}Yb_{0.1}O_{2.95}$, showing that the lowest energy configuration for placement of two Yb and oxygen vacancy defects is a ($M_{Ce}'V_o^{\bullet\bullet}M_{Ce}'$) trimer. Evidence of dopant-vacancy association in $SrCeO_3$ in the literature is limited to one report of mechanical relaxation measurements.[61] However, Phillips et al.[52] also speculate that decreasing unit-cell volume with Y content observed in $SrCe_{1-x}Y_xO_{3-\delta}$ may result from ordering of Y, although occupation on the A-site with Y is also considered, which in turn would lower the vacancy content. Furthermore, lattice-parameter anomalies in $Sr_{1-x}Ce_{0.9}M_{0.1}O_{3-\delta}$ (M = Gd, Yb) solid solutions may be related to defect association, as mentioned previously.[56] By analogy with the oxide-ion conducting systems such as doped CeO_2, a significant amount of defect clustering is expected to lower oxide-ion conductivity as a result of vacancy trapping at lower temperatures and higher dopant levels. The concentration of associated defects is likely to be highly dependent on the thermal history of the sample. This may, in turn, result in variations in experimental activation energies for oxide-ion conduction in $SrCeO_3$-based compositions.

3.5. Water Incorporation and Dopant-Proton Association. As mentioned in the Introduction, mobile protons are incorporated into the perovskite structure on substitution of oxygen vacancies with hydroxyl groups according to reaction 1. The enthalpy of water dissolution (proton incorporation), E_{H_2O}, for the proton-conducting perovskites is known to be exothermic such that the ionic conductivity is dominated by protons at low temperatures and oxygen vacancies at higher temperatures.

The same methodology as used previously for evaluating the energetics of water incorporation in HTPC perovskites[40,41] was employed here to calculate E_{H_2O} for $SrCe_{0.9}Yb_{0.1}O_{2.95}$ according to

$$E_{H_2O} = 2E_{OH} - E_{V_O^{\bullet\bullet}} + E_{PT} \quad (9)$$

where E_{OH} is the energy associated with substitution of O^{2-} with an OH^- group, $E_{V_O^{\bullet\bullet}}$ is the energy needed to create an oxygen vacancy, and E_{PT} is the energy (−11.77 eV) of the gas-phase reaction: $O^{2-} + H_2O = 2OH^-$.[62,63]

The calculated values for E_{OH}, E_{H_2O} (on the O1 and O2 sites), and the O−H bond lengths after relaxation are listed in Table 6. Our favorable value for E_{H_2O} (−1.46 eV) at the O1 site is compatible with experimental thermodynamic values for the enthalpy of water dissolution in $SrCeO_3$-based systems, although the data is sensitive to the dopant type as discussed previously.[4,6] Song et al.[59] derived an E_{H_2O} of −1.70 eV for $SrCe_{0.95}Eu_{0.05}O_{3-\delta}$, whereas Krug et. al.[64] obtained a value of −1.63 eV for $SrCe_{0.95}Yb_{0.05}O_{3-\delta}$; Yajima and Iwahara report a somewhat lower value of E_{H_2O} = −1.36 eV for the Yb-doped phase.[65]

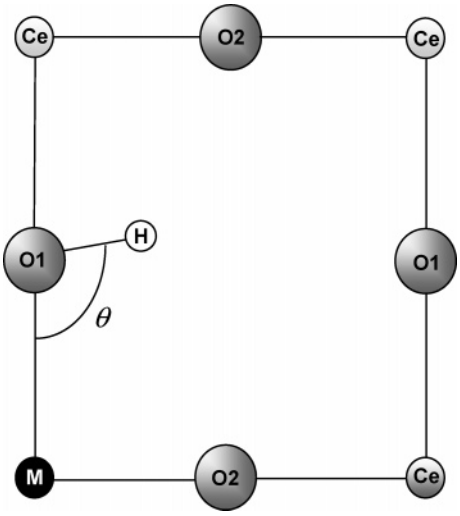

Figure 6. Schematic illustration of an $M_{Ce}'OH_o^{\bullet}$ dopant cluster in the $SrCeO_3$ structure (orthorhombic distortion not represented).

The equilibrium O−H distance is 0.99 Å, similar to that calculated for $BaCeO_3$ by atomistic simulation, and within the range of 0.89−1.05 Å determined in a quantum molecular dynamics study of $BaCeO_3$.[66] Matzke et al.[28] determined a radius for proton motion in $SrCe_{0.95}Yb_{0.05}O_{3-\delta}$ of about 1.1 Å in a quasielastic thermal neutron scattering (QENS) experiment.

Analogous to dopant-vacancy interactions, the proton may also associate preferentially with dopants, leading to possible trapping. Neutron vibrational spectroscopic studies[27] and QENS[28,29] suggest that this occurs in doped $SrCeO_3$ with the OH vibrational modes depending strongly on the dopant cation radius. Atomistic simulation and quantum mechanical simulations also suggest proton-dopant association in the proton-conducting zirconates $AZrO_3$ (A = Ca, Sr, Ba)[38,40,67] in agreement with neutron vibrational and muon-spin relaxation studies.

In the present study, we have calculated the binding energy associated with a cluster comprised of an OH group and adjacent trivalent cations ($M'_{Ce}-OH_o^{\bullet}$) within $SrCeO_3$, in a manner similar to previous studies.[40] A schematic diagram of the ($M'_{Ce}-OH_o^{\bullet}$) dopant cluster with the $OH_o^{\bullet}$ group located on the O1 site is shown in Figure 6. The binding energy of an $M'_{Ce}-OH_o^{\bullet}$ cluster, calculated as the difference between the sum of the isolated defects and the cluster energy, is given by

$$E_{bind} = E(M_{Ce}'-OH_o^{\bullet}) - \{E(M_{Ce}') + E(OH_o^{\bullet})\} \quad (10)$$

The results are shown in Figure 7 as a function of ionic radius. The negative values for the binding energies indicate that $M'_{Ce}-OH_o^{\bullet}$ pair clusters are favorable. In particular, the magnitudes of the $M'_{Ce}-OH_o^{\bullet}$ binding energies are consider-

(61) Zimmermann, L.; Bohn, H. G.; Schilling, W.; Syskakis, E. *Solid State Ionics* **1995**, *77*, 163.
(62) Wright, K.; Freer, R.; Catlow, C. R. A. *Phys. Chem. Miner.* **1995**, *20*, 500.
(63) Catlow, C. R. A. *J. Phys. Chem. Solids* **1977**, *28*, 1131.
(64) Krug, F.; Schober, T.; Springer, T. *Solid State Ionics* **1995**, *81*, 111.
(65) Yajima, T.; Iwahara, H. *Solid State Ionics* **1992**, *50*, 281.
(66) Münch, W.; Seifert, G.; Kreur, K. D.; Maier, J. *Solid State Ionics* **1994**, *70−71*, 278.
(67) Islam, M. S.; Davies, R. A.; Gale, J. D. *Chem. Commun.* **2001**, 661.

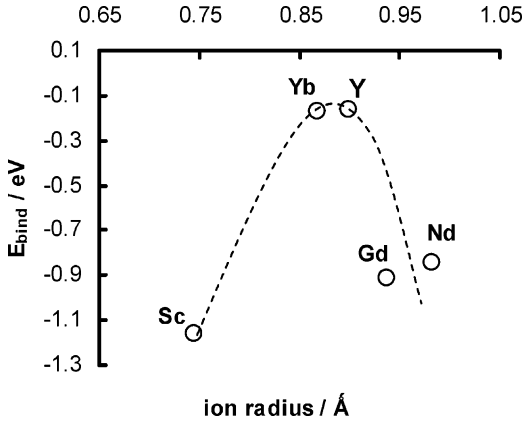

Figure 7. Calculated binding energies of ($M_{Ce}'OH_o^{\bullet}$) pair clusters in $SrCeO_3$ as a function of dopant ionic radius.

Table 7. Calculated Binding Energies, Interatomic Distances, and Bond Angles of $M'_{Ce}-OH_o^{\bullet}$ Clusters in $SrCeO_3$

cation	ionic radius (Å)	E (eV)	M···H (Å)	M···O (Å)	M−O−H (deg)
Ce^{4+}	0.87		2.860	2.429	106.04
Sc^{3+}	0.74	−1.16	2.295	2.408	71.39
Yb^{3+}	0.87	−0.17	3.286	2.468	142.53
Y^{3+}	0.90	−0.16	3.328	2.494	144.56
Gd^{3+}	0.94	−0.91	2.914	2.560	101.08
Nd^{3+}	0.98	−0.84	2.782	2.593	94.28

ably lower for Y^{3+} and Yb^{3+} in comparison to those of the other dopants. Since these dopants are most often associated with high protonic conductivity in the $SrCeO_3$ system,[16,52,68] it follows that the lower conductivity of other doped systems (e.g., Sc) may partly result from appreciable dopant-proton association; i.e., the highest and lowest proton mobilities are predicted for Y/Yb- and Sc-doped $SrCeO_3$, respectively. Our calculated binding energies are also similar to an experimental value for the proton "trapping" energy of about −0.4 eV for Yb-doped $SrCeO_3$ obtained from QENS experiments.[29] The atomistic calculations thus support the experimental spectroscopic evidence of proton-dopant association.

The trend found in Figure 7 suggests the importance of ion-size and elastic-strain effects, in addition to electrostatic terms, in which the binding energy is dependent upon the ion size "mis-match" between host and dopant. This causes local perturbation, and the expectation of a minimum when the ionic radii are approximately the same. This is borne out here with the lowest binding energies for Yb^{3+} (0.87 Å) and Y^{3+} (0.90 Å) on the host Ce^{4+} site (0.87 Å), with the greatest ion-size mismatch for small Sc^{3+} (0.74 Å) and large Nd^{3+} (0.98 Å). These results and elastic strain arguments are analogous to studies of Catlow[36] and Kilner[69] on fluorite-structured oxides (e.g., doped CeO_2), and to our recent work on doped $LaGaO_3$,[37] in which the minimum in the binding energy for dopant-vacancy clusters occurs when the host and dopant ionic radii are very similar.

The interatomic distances between the M dopant and both the oxygen and proton of the hydroxyl unit in the $M'_{Ce}-OH_o^{\bullet}$ cluster have been analyzed and are shown in Table 7 and Figure 8; in addition, Table 7 lists the angle (θ in Figure 6) formed between the OH group and M dopant. The analysis reveals that the distance between the dopant and the hydroxyl oxygen (M−O) increases by a small amount approximately as a function of the M ionic radius. In contrast, the distance between M and the proton (M−H) and corresponding $M'_{Ce}-O-H$ angle is greatest for the Yb and Y dopants, and mirrors the variation in binding energy (Figure 7). Hence, our simulations appear to show a correlation among the lowest $M'_{Ce}-OH_o^{\bullet}$ binding energies and longest $M'_{Ce}-H$ distances with the highest proton conductivities.

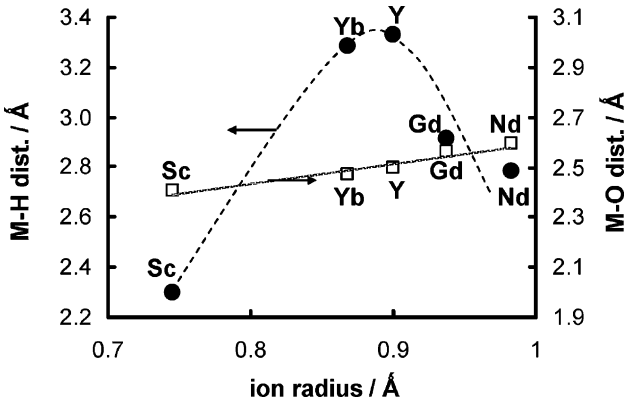

Figure 8. Interatomic distances between trivalent dopant and oxygen (M−O) and between dopant and proton (M−H) in the ($M_{Ce}'OH_o^{\bullet}$) pair cluster as a function of dopant ionic radius.

3.6. Redox Reactions. An understanding of the redox behavior of HTPC materials is critical for defining the conditions in which various conductivity regimes may be exploited. Experimental determination and interpretation of the defect equilibria of these systems is rather involved due to the numerous possible conducting species (electron, hole, proton, and oxide ion) and their respective dependencies on temperature and atmosphere. A number of authors have used numerical methods to examine concentration profiles of electronic and ionic defects in doped $SrCeO_3$ in equilibrium with two gases (pO_2, pH_2O).[21,70,71] Atomistic simulation of the redox behavior is also a useful tool in assisting the interpretation of the experimental data, as has been shown previously.[40,41] Moreover, our calculations allow dopant-vacancy interaction to be incorporated in the analysis, which has not yet been considered for other defect calculations of $SrCeO_3$.

Reduction was considered in accordance with reaction 3; modeling of the electron center involved the creation of a Ce^{3+} ion as a small polaron species on the B cation sublattice in a similar approach to that used previously for $BaCeO_3$ and CeO_2.[41,44] We may note that recent work indicates transport in H_2-containing atmospheres may be protonic rather than n-type.[52,72] Oxidation involved the modeling of the hole center ($h^{\bullet}$) as O^-, in accordance with previous simulations in oxide systems.[41] The energies of the redox reactions in the lattices of $SrCeO_3$ and $SrCe_{0.9}Yb_{0.1}O_{2.95}$ were then calculated, employing these isolated electronic terms and the relevant free-ion terms (Table 8).

(68) Iwahara, H. *Solid State Ionics* **1988**, *28−30*, 99.
(69) Kilner, J. A. *Solid State Ionics* **2000**, *129*, 13.
(70) Poulsen, F. W. *J. Solid State Chem.* **1999**, *143*, 115.
(71) Bonanos, N.; Poulsen, F. W. *J. Mater. Chem.* **1999**, *9*, 431.
(72) Bonanos, N. *Solid State Ionics* **2001**, *125*, 265.

Table 8. Calculated Energies of Redox Reactions

	energy (eV/electronic defect)	
redox process	$SrCeO_3$	$SrCe_{0.9}Yb_{0.1}O_{2.95}$
oxidation reaction 2	2.25	2.10
reduction reaction 3	5.00	4.16

The calculated redox energies compare well with values obtained from conductivity measurements of $SrCe_{0.95}Yb_{0.05}O_{3-\delta}$ of 1.6 and 4.8 eV for oxidation and reduction enthalpies, respectively.[20] Although these are not explicit electronic structure methods, our calculated band gap (~2.7 eV) for $SrCeO_3$ is consistent with the limited available data of Kosacki and Tuller,[20] where a value of 3.2 eV is derived.

The present calculations thus confirm that p-type is the dominant mechanism for electronic conduction in $SrCeO_3$-based systems over a wide range of conditions. As pointed out recently by Bonanos,[72] investigation of the nature of the p-type carrier in the HTPC systems is limited. A recent report relates electronic conduction and hydrogen permeability in $SrCe_{0.95}Eu_{0.05}O_{3-\delta}$ to mixed valent Eu species.[59] The present data show that the formation of hole species in oxidative atmospheres is a viable process. The observed conductivity at low pO_2 increases only below ca. 10^{-16} atm in accordance with the high value calculated for reduction. In comparison with the results of previous simulation studies, $SrCeO_3$ is expected to be more stable to reduction than the $BaCeO_3$ system but less stable than the zirconate perovskites,[40,41] which is consistent with expected reduction potentials of the Ce(IV) and Zr(IV) ions.

4. Conclusions

Computer simulation techniques have been used to probe the energetics of defects, dopants, and clustering in the proton-conducting $SrCeO_3$ material at the atomic level. The results are relevant to the electrochemical applications of the cerate system (SOFCs, sensors, separation membranes) and are summarized as follows.

(1) The potential model first reproduces the highly distorted perovskite structure of $SrCeO_3$. Supercell structures were constructed to determine the lowest energy configuration for the doped system, $SrCe_{0.9}Yb_{0.1}O_{2.95}$, with the most favorable configuration consisting of a ($Yb_{Ce}'V_o^{\bullet\bullet}Yb_{Ce}'$) nearest-neighbor trimer arrangement.

(2) Calculated energies for intrinsic atomic defects are relatively high, with the most favorable found to be the SrO vacancy pair. The lowest energy redox process is oxidation with the formation of holes (modeled as an O^- center) in accordance with the observation of p-type conductivity at high pO_2 and with experimental oxidation enthalpies.

(3) Trivalent dopant substitution on the Sr site at the dilute limit in $SrCe_{0.9}Yb_{0.1}O_{3-\delta}$ (via $V_o^{\bullet\bullet}$ consumption) is calculated to be of lower energy than substitution on the Ce site ($V_o^{\bullet\bullet}$ creation), particularly for Nd^{3+} and Gd^{3+}. Dopants may, therefore, occupy both Sr and Ce sites in low concentrations. This is compatible with the premise that the absence of protonic conductivity at low doping levels is associated with amphoteric behavior or dopant "partitioning" over both Sr and Ce sites where oxygen vacancies are not formed, which, in turn, inhibits proton uptake.

(4) Dopant-vacancy association is predicted to be favorable, especially for neutral ($M_{Ce}'V_o^{\bullet\bullet}M_{Ce}'$) trimers and for the Sc^{3+} dopant. These clusters may be important as precursors to possible short-range ordering or "nano-domain" formation at higher dopant regimes, which warrants further experimental investigation.

(5) The pathway for oxygen migration is proposed as a curved trajectory with an asymmetric energy distribution resulting from the pronounced distortion of the $SrCeO_3$ perovskite lattice.

(6) The enthalpy of water dissolution is calculated to be exothermic and is consistent with the available experimental thermodynamic data. Binding energies for ($M'_{Ce}-OH_o^{\bullet}$) pairs are predicted to be favorable, with the strongest association for Sc^{3+}. The Y^{3+} and Yb^{3+} dopants have the lowest binding energies (weakest association) and the largest $M'_{Ce}-H$ distances. This may be linked to why these two cations are the most commonly used acceptor dopants in $SrCeO_3$ for high proton mobility and conductivity.

Acknowledgment. We would like to thank the ESF OSSEP programme (Optimisation of Solid State Electrochemical Processes for Hydrocarbon Oxidation) for financial support. Assistance from Dr. Julian Tolchard is also appreciated.

CM047976L